Electronic and Structural Properties of Highly Aluminum Ion Doped TiO₂ Nanoparticles: A Combined Experimental and Theoretical Study

Desireé M. de los Santos,[a] Teresa Aguilar,[a] Antonio Sánchez-Coronilla,*[a] Javier Navas,*[a] Norge Cruz Hernández,[b] Rodrigo Alcántara,[a] Concha Fernández-Lorenzo,[a] and Joaquín Martín-Calleja[a]

This study presents the experimental and theoretical study of highly internally Al-doped TiO₂ nanoparticles. Two synthesis methods were used and detailed characterization was performed. There were differences in the doping and the crystallinity, but the nanoparticles synthesized with the different methods share common features. Anatase to rutile transformation occurred at higher temperatures with Al doping. X-ray photoelectron spectroscopy showed the generation of oxygen vacancies, which is an interesting feature in photocatalysis. In turn, the band-gap energy and the valence band did not change appreciably. Periodic density functional calculations were performed to model the experimentally doped structures, the formation of the oxygen vacancies, and the band gap. Calculation of the density of states confirmed the experimental band-gap energies. The theoretical results confirmed the presence of Ti⁴⁺ and Al³⁺. The charge density study and electron localization function analysis indicated that the inclusion of Al in the anatase structure resulted in a strengthening of the Ti—O bonds around the vacancy.

1. Introduction

TiO₂ is one of the most commonly used semiconductors in photocatalytic and photovoltaic applications because of its different properties, such as low cost, low toxicity, chemical stability, and so on.[1,2] It is possible to find several examples of its use as a photocatalyst, including its use to obtain H₂ from H₂O (water splitting),[3,4] the conversion of CO₂ into fuel by using H₂O[5–8] or H₂,[9,10] and the photodegradation of dyes and organic compounds.[11,12] It is used in photovoltaic applications as a semiconductor in dye-sensitized solar cells (DSSCs).[13–17] Doping TiO₂ is an interesting strategy used to improve its properties as a semiconductor and, thus, its efficiency in many applications. Thus, studies of the photocatalytic activity of TiO₂ doped with iron,[18,19] carbon,[20,21] bismuth,[22] neodymium,[23] iodine,[24] and copper[25] have been performed. The performance of TiO₂ in DSSCs has been improved with dopants such as fluorine,[26] silver,[27] tin,[28] aluminum,[29] tungsten,[29] nitrogen,[30] niobium,[31] ytterbium,[32] and copper.[33]

However, only a few studies on the doping of TiO₂ with Al have been performed, and in these cases, the percentage of doping was low, at around 3 wt % (Al/TiO₂), which is 10 at %, the maximum doping obtained by using dissolution methods for synthesis.[34–38] For example, Kang reported doping of up to 10 at % by using a solvothermal method,[37] and Zaki et al. reported doping of 3 at % with different ions by using a sol–gel method of synthesis.[38]

Fundamental understanding of the interaction of Al with TiO₂ is required to rationalize the experimental information in this topic, and first-principle calculations have been shown to be an interesting tool in the theoretical study of doped rutile and anatase TiO₂.[39,40]

In this paper, we introduce a combined study of Al-doped TiO₂ from experimental and theoretical point of views. Al-doped TiO₂ nanoparticles were synthesized by using two methods (named methods M1 and M2) to produce levels of doping up to 20.0 and 15.4 at % while maintaining the crystallinity of the samples in most cases. The samples had low crystallinity only at high levels of doping and low annealing temperatures. The synthesized samples were extensively characterized through physicochemical methods, which enabled the study of the evolution of the properties of the nanoparticles as a function of the annealing temperature, the percentage of doping, and the method of synthesis used.[41] With both methods of synthesis, the formation of the rutile phase was delayed if the doping was increased, so the anatase phase was predominant in most cases, and therefore, this was the structure modeled from a theoretical viewpoint. In turn, there was evi-

[a] D. M. de los Santos, T. Aguilar, Dr. A. Sánchez-Coronilla, Dr. J. Navas, Dr. R. Alcántara, Dr. C. Fernández-Lorenzo, Prof.Dr. J. Martín-Calleja
Department of Physical Chemistry, Cádiz University
11510 Puerto Real, Cádiz (Spain)
Fax: (+ 34) 956 016 471
E-mail: antonio.coronilla@uca.es
        javier.navas@uca.es

[b] Dr. N. Cruz Hernández
Department of Applied Physics I, Seville University
41012 Seville (Spain)

🖳 Supporting Information for this article is available on the WWW under http://dx.doi.org/10.1002/cphc.201402071.

dence of the generation of oxygen vacancies in the structure after doping, which is an interesting characteristic for the use of the synthesized nanoparticles in photocatalytic applications. From experimental observations, periodic density functional theory (DFT-periodic) calculations were performed to model the experimentally observed doped structures. The Vienna Ab Initio Simulation Package[42–45] with the projector-augmented wave method[46,47] was used. The $Al_2Ti_{62}O_{127}$ (191 atoms, Al doping of 3.1 at%), $Al_2Ti_{30}O_{63}$ (94 atoms, Al doping of 6.3 at%), and $Al_2Ti_{14}O_{31}$ (47 atoms, Al doping of 12.5 at%) structures were selected as representative models within the wide range of experimental Al-doped concentrations. The chosen structures were studied by considering that the generation of the oxygen vacancies would simulate the experimental stoichiometries of interest by simulating the doping levels at which Al doping generates oxygen vacancies and at which the anatase structure is not very distorted. The presence of Al^{3+} and Ti^{4+} in the structures is shown by X-ray photoelectron spectroscopy (XPS) and confirmed by Bader charge analysis.[48–50] Moreover, charge density and electron localization function[51–55] shed light on the bonding character of Al-doped TiO_2. Thus, there was strengthening of the Ti—O bond around the vacancy for the Al-doped TiO_2 sample relative to the same bond in undoped TiO_2. The study of density of states and projected density of states clearly indicated the negligible contribution of the sp states of Al relative to the contribution of the 3d and 2p states of Ti and O, respectively, in the samples. Thus, the band gap of Al-doped TiO_2 remained similar to that of anatase in which the 3d and 2p states of Ti and O, respectively, play crucial roles in the band-gap energy, as observed experimentally.

2. Results and Discussion

2.1 Inductively Coupled Plasma Atomic Emission Spectroscopy

The percentage of Al in the samples synthesized by using both methods was obtained from inductively coupled plasma atomic emission spectroscopy (ICP-AES). Table 1 shows the values of the weight percentage of Al calculated as the arithmetic average of the value obtained for each annealing temperature. For method M1, the real percentage of Al was greater than the theoretical one added during the synthesis. The reason for this was the unwanted hydrolysis of titanium isopropoxide with ambient water, which produced a loss of synthesized TiO_2. For this reason, the percentage of Al in the samples synthesized by method M1 was greater than that in the samples obtained with method M2. In turn, from the ICP-AES results, the Al atomic percentage, that is, the ratio Al/(Al+Ti), was calculated (see Table 1). The maximum atomic percentage was 20 at%, which is higher than the values reported in the literature by using dissolution methods of synthesis. Generally, the common maximum values were about 10 at%.[34–38] For example, Kang et al. obtained doping up to 10 at% by using a solvothermal method.[37] Moreover, the empirical formula was obtained by considering the XPS results (see below).

Table 1. Real weight percentage of Al versus TiO_2, atomic/molar percentage of Al [Al/(Al+Ti)] obtained by ICP-AES, and experimental stoichiometric formula obtained from ICP-AES and XPS and by considering oxygen vacancies.

Method M1 Theoretical Al/TiO_2 [wt%]	Real Al/TiO_2 [wt%]	Al/(Al+Ti) [at%]	Formula
pure TiO_2	<0.10[a]	0.0	TiO_2
1.0	1.36±0.02	3.9	$Al_2Ti_{49}O_{101}$
2.0	2.32±0.06	6.7	$Al_2Ti_{28}O_{59}$
2.5	3.12±0.16	8.7	$Al_2Ti_{21}O_{45}$
5.0	5.07±0.23	14.3	$Al_2Ti_{12}O_{27}$
7.5	7.37±0.33	20.0	$Al_2Ti_8O_{19}$

Method M2 Theoretical Al/TiO_2 [wt%]	Real Al/TiO_2 [wt%]	Al/(Al+Ti) [at%]	Formula
pure TiO_2	<0.10[a]	0.0	TiO_2
1.0	0.59±0.07	1.7	$Al_2Ti_{114}O_{231}$
2.0	1.08±0.11	3.1	$Al_2Ti_{62}O_{127}$
2.5	1.90±0.18	5.4	$Al_2Ti_{35}O_{73}$
5.0	3.20±0.22	9.1	$Al_2Ti_{20}O_{43}$
7.5	5.53±0.23	14.3	$Al_2Ti_{12}O_{27}$
10.0	5.90±0.30	15.4	$Al_2Ti_{11}O_{25}$

[a] Percentage lower than the detection limit of the analytical method.

In the following discussions of the results obtained from other characterization techniques, the Al atomic percentage will be used to name the samples synthesized to simplify the comparison between both methods of synthesis.

2.2 X-ray Diffraction

Figures S1 and S2 (see the Supporting Information) show the patterns obtained for the samples synthesized by using both methods of synthesis described above. The most important peaks of the anatase and rutile phases were assigned in these patterns. In accordance with the references for the two typical crystalline phases of TiO_2, JCPDS 21-1272 for the anatase phase and JCPDS 21-1276 for the rutile phase, the peaks at $2\theta = 25.28$ and $27.42°$ correspond to the main signals of both phases, the reflection of the anatase (101) and rutile (110) planes, respectively.[56] In the diffractograms, only the peaks of the anatase and rutile phases are observed in the doped samples. The patterns do not show evidence for the presence of any crystalline phases formed by Al species, which leads us to believe that the Al ions were uniformly distributed in the TiO_2 crystals. This result is consistent with the results obtained by using other characterization techniques such as Raman spectroscopy and XPS, as we report below. At similar levels of doping, the crystallinity of the samples obtained by method M2 was worse than that of samples obtained by method M1. Figure S1 and S2 show diffractograms with a worse signal/noise ratio for method M2 at similar levels of doping. Even for the samples with a level of doping similar to or greater than 9.1 at%, annealed at 773 K, there was no signal observed for any crystalline phase.

From the XRD diffractograms, a semiquantitative assessment was made of the percentage of the anatase and rutile phases in the synthesized samples and some properties of the samples, such as their mean crystal size, unit cell volume, and specific surface area. The mass fraction of the anatase phase in the samples was calculated by Equation (1):

$$f_A = \left(1 + \frac{1.26 I_R}{I_A}\right)^{-1} \tag{1}$$

in which f_A is the mass fraction of the anatase phase and I_R and I_A are the intensities of the reflection of the (110) and (101) planes for the rutile and anatase phases, respectively.[57] Table 2 shows the mass fractions obtained for the anatase and rutile phases by using methods M1 and M2, respectively. With method M1, the anatase phase was usually predominant at annealing temperatures of 773 and 973 K, whereas the rutile phase was predominant for temperatures of 1173 K, with the single exception of the sample of pure TiO_2 annealed at 973 K, for which the predominant phase was rutile. In the samples doped between 14.3 and 20.0 at%, the crystallinity was low, as observed in the diffractograms (Figure S1). In turn, for method M2, in the samples annealed at 773 and 973 K, the anatase phase was predominant, except for the sample of pure TiO_2 annealed at 973 K, as was the case for method M1. Likewise, in the samples annealed at 773 K with doping levels of 9.1, 14.3, and 15.4 at%, no crystalline phase was detected. The samples annealed at 1173 K had a dominant rutile phase for doping up to and including 9.1 at%, whereas for the samples with levels of doping of 14.3 and 15.4 at% the predominant phase was anatase again. Thus, in both methods, the transition from anatase to rutile in the Al doped samples occurred at higher temperatures, so the anatase phase was predominant in most of the samples.

Figure 1a shows the evolution of the mass fraction of the anatase phase versus the level of doping for the different annealing temperatures. It shows how method M2 produces a greater proportion of the anatase phase than method M1 under the same conditions. The limit is observed at 1173 K and at high levels of doping, for which the rutile phase is predominant for method M1 and the anatase phase is predominant for method M2.

The average crystallite size (t) was calculated from the Scherrer equation [Eq. (2)]:

$$t = \frac{0.9\lambda}{\beta \cos\theta} \tag{2}$$

in which θ is the diffraction angle, β is the full-width-at-half-maximum (FWHM) in radians, and λ is the wavelength of the X-ray radiation, that is, $CuK\alpha$ (0.154 nm).[58] Table 2 shows the values of t for the samples synthesized by using both methods, whereas Figure 1b shows the evolution of t in relation to the annealing temperature and doping percentage. The average crystallite size values were obtained for the predominant phase of each sample by using the major peak of the patterns, that is, the (110) and (101) planes for the rutile and anatase phases, respectively. To obtain the best value of β and therefore that of t, an adequate baseline correction was applied. From the values obtained for a given annealing temperature, the higher the doping level, the lower the value of t. The introduction of an Al^{3+} ion into the structure can create structural

Table 2. Anatase and rutile mass fraction, average crystallite size, unit cell volume, and specific surface area of samples synthesized by using both methods obtained by XRD.

Method M1

Al/(Al+Ti) [at%]	T_a [K]	f_A [wt%]	f_R[a] [wt%]	t[b] [nm]	V[b] [Å³]	s_a[b] [m²g⁻¹]
	773	75.5	24.5	15.9	140.5	99.6
0.0	973	7.6	92.4	55.9	62.3	25.2
	1173	0.0	100.0	59.6	62.7	23.8
	773	65.2	34.8	7.6	135.7	202.8
3.9	973	71.2	28.8	20.7	137.0	75.7
	1173	1.8	98.2	52.7	61.8	26.8
	773	67.1	32.9	7.5	135.3	208.3
6.7	973	78.3	21.7	13.9	138.4	114.3
	1173	15.6	84.4	57.7	62.3	25.9
	773	63.1	36.9	5.7	132.7	270.7
8.7	973	65.4	34.6	12.5	140.5	129.7
	1173	17.7	82.3	51.2	62.1	28.1
	773	53.5[c]	46.5[c]	5.4[c]	111.5[c]	244.2[c]
14.3	973	50.6	49.4	8.8	138.0	184.7
	1173	5.8	94.2	47.1	62.9	31.9
	773	50.4[c]	49.6[c]	4.6[c]	132.7[c]	342.4[c]
20.0	973	52.6	47.4	7.5	130.9	208.7
	1173	13.1	86.9	49.7	62.7	30.1

Method M2

Al/(Al+Ti) [at%]	T_a [K]	f_A [wt%]	f_R[a] [wt%]	t[b] [nm]	V[b] [Å³]	s_a[b] [m²g⁻¹]
	773	91.6	8.4	10.3	135.3	148.0
0.0	973	7.8	92.2	62.6	62.7	22.7
	1173	0.0	100.0	64.0	62.0	21.9
	773	92.5	7.5	8.8	138.3	178.8
1.7	973	89.7	10.3	25.9	133.8	58.8
	1173	0.0	100.0	63.9	62.9	22.4
	773	100.0	0.0	7.3	135.9	211.6
3.1	973	97.4	2.6	22.0	135.9	70.5
	1173	2.4	97.6	66.3	62.3	21.4
	773	100.0	0.0	7.0	141.9	231.7
5.4	973	100.0	0.0	14.6	137.0	107.4
	1173	27.8	72.2	61.7	62.4	23.2
	773	_[c]	_[c]	_[c]	_[c]	_[c]
9.1	973	91.4	8.6	14.6	138.4	109.6
	1173	27.5	72.5	59.7	62.4	24.2
14.3	973	100.0	0.0	8.8	137.0	183.2
	1173	72.4	27.6	48.8	139.2	33.5
	773	_[c]	_[c]	_[c]	_[c]	_[c]
15.4	973	100.0	0.0	8.2	133.8	192.7
	1173	65.7	34.3	43.9	134.5	36.1

[a] f_R [wt%] = 100 − f_A [wt%]. [b] Values calculated for the predominant phase. [c] Low crystallinity.
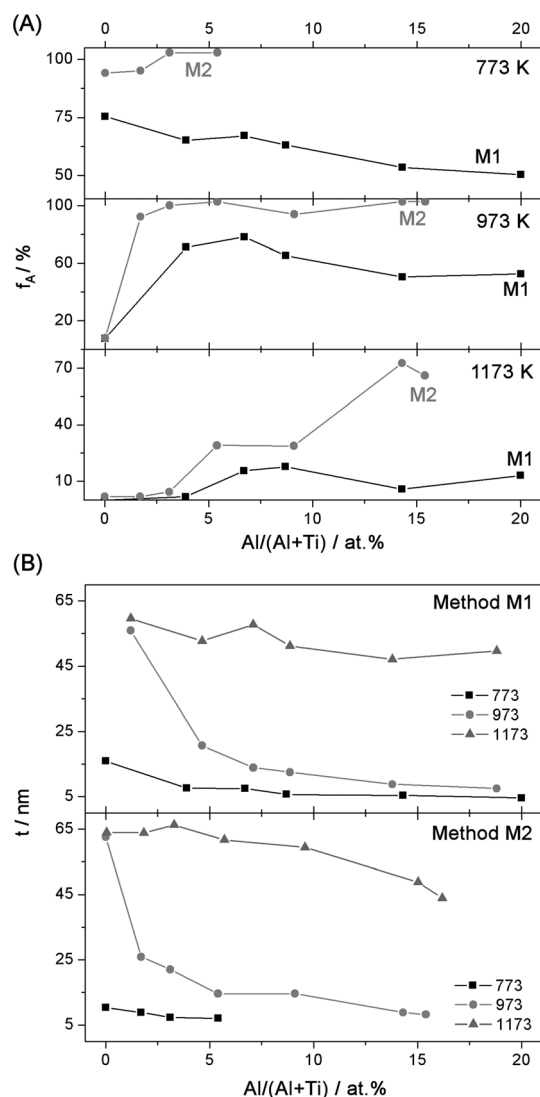
Figure 1. a) Evolution of the anatase mass fraction, f_A, and b) the average crystallite size, t, as a function of atomic percentage of Al.

distortions that break the crystal continuity, which thereby results in smaller average crystallite sizes.[59,60] In turn, for any given doping level, the value of t grows if the annealing temperature increases, because of sintering of the nanocrystals.

Furthermore, the specific surface area (s_a) was calculated from the XRD patterns by using Equation (3):

$$s_a = \frac{6}{t\rho} \tag{3}$$

in which ρ is the density obtained by means of XRD [Eq. (4)]:

$$\rho = \frac{nM}{NV} \tag{4}$$

in which N is the Avogadro number, M is the molecular weight ($n = 2$ for the rutile phase and $n = 4$ for the anatase phase), and V is the unit cell volume calculated from Equation (5):

$$V = ac^2 \tag{5}$$

in which a and c are the lattice parameters and $a = b \neq c$ for the rutile and anatase phases.[61] The values of a and c were obtained from the XRD patterns by using the two peaks with the highest intensity with the aid of Equation (6):[59]

$$\frac{1}{d^2} = \frac{h^2 + k^2}{a^2} + \frac{l^2}{c^2} \tag{6}$$

in which h, k, and l are the Miller indexes of the planes used and d is the interplanar distance. In turn, the molecular weight was calculated by considering the empirical formula obtained from the ICP-AES and XPS results (see below). The values of V and s_a obtained for the samples synthesized by using the two synthesis methods are shown in Table 2. Typically, we observed lower values of s_a if the predominant phase was rutile; that is, t was higher for the rutile phase than for the anatase phase. As discussed above, Al doping delays the transition from anatase to rutile until higher temperatures, so high values of s_a are found in samples synthesized with higher doping levels.

2.3 X-ray Photoelectron Spectroscopy

Figure 2a shows the Ti 2p spectra for pure TiO_2 synthesized by using both methods, for 6.7 and 14.3 at% Al-doped TiO_2 synthesized by method M1, and for 3.1 and 9.1 at% Al-doped TiO_2 synthesized by method M2. These samples were chosen because they are considered representative of the nanoparticles synthesized by both methods. There is close alignment between the Ti 2p peaks for the doped and pure samples in both methods. The binding energies (BEs) of Ti $2p_{3/2}$ and Ti $2p_{1/2}$ were around 458.5–458.7 and 464.2–464.4 eV, respectively, for all the samples synthesized. These values are consistent with those reported in the literature. Values for the BE for Ti $2p_{3/2}$ of 458.66, 457.13, 455.34, and 453.86 eV have been reported for Ti^{IV}, Ti^{III}, Ti^{II}, and Ti^0, respectively.[62] For all the synthesized samples, the FWHM of the Ti $2p_{3/2}$ peak was around 0.95 eV, which is also consistent with values reported in the literature for Ti^{IV}.[38,63,64] Moreover, the separation between the BEs of Ti $2p_{3/2}$ and Ti $2p_{1/2}$ was around 5.6–5.7 eV in all cases. These values are also in agreement with previous results for Ti^{IV}.[36] Considering these results, Ti^{IV} was the dominant oxidation state of Ti in the pure and doped samples synthesized by using both methods. The typical presence of Ti^{3+} in TiO_2[65] was negligible in our samples, as observed from the XPS spectra. This situation was also reported previously.[27,36,65,66]

Moreover, the BE of Al $2p_{3/2}$ was around 74.0 eV for all the samples synthesized by using both methods, which is consistent with values of Al^{III} reported previously.[35,63,64] Figure 2b shows the XPS spectra of one sample synthesized by using both methods (which are considered representatives of the synthesized samples) and two reference samples, $Al(OH)_3$ and Al_2O_3. The Al $2p_{3/2}$ peak for both samples is coincident with that in the Al_2O_3 spectrum. The Al $2p_{3/2}$ peak for $Al(OH)_3$ is

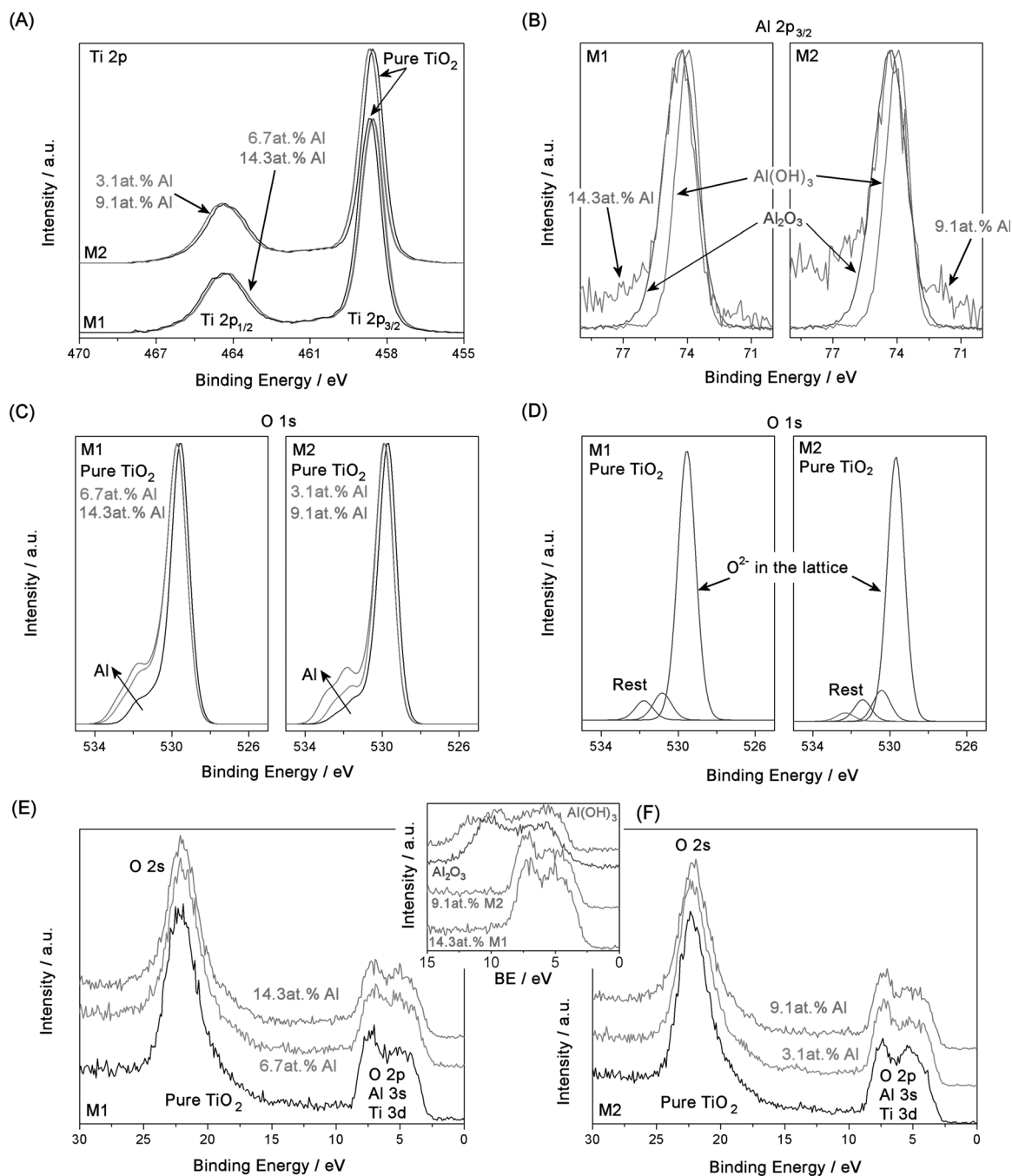**Figure 2.** XPS spectra for samples synthesized by both methods: a) Ti 2p; b) Al 2p, including Al(OH)$_3$ and Al$_2$O$_3$ samples; c) O 1s; d) O 1s, showing the contributions of different O in the samples. e) Valence band for samples synthesized by method M1 and f) valence band for samples synthesized by method M2.

0.4 eV lower than the BE value of the synthesized samples and Al$_2$O$_3$.

Thus, from the XPS spectra we can conclude that in the doped samples synthesized by using both methods the Al is found as Al^{III} in a situation that is similar to Al^{3+} in an oxidic matrix. In turn, the incorporation of Al^{III} into the TiO$_2$ structure does not involve changes in the oxidation state of Ti, which remains as Ti^{IV}. However, the incorporation of Al^{III}, which substitutes Ti^{IV}, involves a loss in the local charge neutrality in the TiO$_2$ lattice. Thus, oxygen vacancies are produced, which is consistent with previous reports.[57,66] Considering the ICP-AES

reported before and the production of oxygen vacancies to maintain charge neutrality, the empirical formula of the samples synthesized was calculated and is shown in Table 1. The oxygen vacancies were considered in the theoretical simulation exposed below.

The O 1s spectra were also recorded. Figure 2c shows several spectra for samples synthesized with both methods. The peak shape is asymmetrical, which was previously observed for TiO$_2$ doped with dopants such as Au,[67] Al,[38] Ag,[68] and Cu.[68] Usually, the asymmetry of the O 1s peak is explained according to the presence of several contributions to the signal. The

presence of O^{2-} in the TiO_2 lattice is undeniable, but the assignment of the other signals is not clear. These other contributions are usually assigned to adsorbed species, such as hydroxyl groups,[69] water,[70] and carboxylate species.[71] Figure 2d shows the XPS spectra for O1s of pure TiO_2 synthesized by using both methods. In these spectra, we can compare the different contributions to the O1s signal. We can observe that the sample synthesized by method M1 shows three contributions, whereas the sample synthesized by using method M2 shows four components. So, probably the samples synthesized by using method M2 have more surface defects that are possible active centers for adsorption; other contributions of O were also found (named "rest" in Figure 2d). For example, the adsorption of carboxylate species can generate one or two signals depending on the adsorption process.[72] For all the doped samples synthesized with both methods, the O1s spectra are similar to the previous case, with four components to the signal. Moreover, Figure 2c shows the XPS spectra for samples synthesized with both methods. These spectra lead to two points of discussion. First, a shift in the peak assigned to O^{2-} in the lattice towards a slightly higher BE is observed in doped samples with regard to pure TiO_2. This might suggest a slightly different state for the oxide[73] or possible small differences in the oxidation state of the O in the lattice due to the vacancies produced upon introduction of the dopant, as will be discussed below by using theoretical modeling. Second, we can observe that the contributions of the adsorbed species in the samples increase with the percentage of dopant for both methods. This could be explained by the formation of oxygen vacancies with doping, which can involve an increase in the number of surface hydroxyl groups. Surface hydroxyl groups can react with photogenerated gaps in a photocatalytic reaction, which inhibits the recombination of the electron-gap pair and enhances charge transfer.[74] Moreover, this can lead to the production of hydroxyl radicals, a good oxidizing agent in organic compound degradation.[75]

Finally, the valence band was recorded for all the samples synthesized. Figure 2e shows the contributions of Ti3d, Al3s, O2p, and O2s to the valence band of pure TiO_2 and two doped samples, considered as representatives, synthesized by

method M1. Likewise, Figure 2f shows the equivalent spectra of samples synthesized by method M2. We can observe that the valence bands for the pure and doped samples are similar. If doping was to have a significant effect, this would happen in the zone between 15 eV and the Fermi level, in the areas of Ti3d, Al3s, and O2p. We can observe no significant difference in this zone of the XPS spectra between the pure and doped samples for both methods. The inset between Figure 2e and 2f shows the spectra of two doped samples (one synthesized with method M1 and another with method M2) and the spectra of the valence band of Al_2O_3 and $Al(OH)_3$, used as references. We can observe a zone between 8.5 and 12.5 eV in which a great contribution to the valence band is observed for Al_2O_3 and $Al(OH)_3$, but this contribution is not observed in the synthesized doped samples. So, the contribution of Al to the valence band is practically negligible. Furthermore, Figure 2e,f shows how the valence band maximum is similar in all cases, which suggests that the variations in band-gap energy will be small, as will be discussed in depth below with the use of the results obtained by UV/Vis spectroscopy in the diffuse reflectance mode.

2.4 Raman Spectroscopy

The main crystalline phases of TiO_2 showed Raman-active modes. The anatase phase showed six active modes at 144 (E_g), 197 (E_g), 399 (B_{1g}), 519 ($A_{1g} + B_{1g}$), and 639 cm^{-1} (E_g).[76] The rutile phase showed four active vibrational modes at 143 (B_{1g}), 447 (E_g), 612 (A_{1g}), and 826 cm^{-1} (B_{2g}).[77] From spectra obtained (see Figure S3 and S4), and considering the active modes noted before, the main phase in the samples synthesized was deduced qualitatively. Table 3 shows the predominant phase for all the samples synthesized by using both methods. We can observe how the transition from anatase to rutile occurs at higher temperatures as the doping level increases. Moreover, no evidence of any crystalline phase formed by Al species was found. Thus, the results obtained from the Raman spectra are consistent with the XRD results detailed above. In turn, the samples synthesized by method M2 have worse crystallinity, as reported in the XRD results.

Table 3. Predominant phase according to Raman spectra for methods M1 and M2.

Method M1

T_a [K]	Al/(Al+Ti) [at%]					
	0.0	3.9	6.7	8.7	14.3	20.0
773	anatase	anatase	anatase	anatase	low crystallinity	low crystallinity
973	rutile	anatase	anatase	anatase	anatase/rutile (40% < fA < 60%)	anatase/rutile (40% < fA < 60%)
1173	rutile	rutile	rutile	rutile (40% < f_A < 60%)	rutile	rutile

Method M2

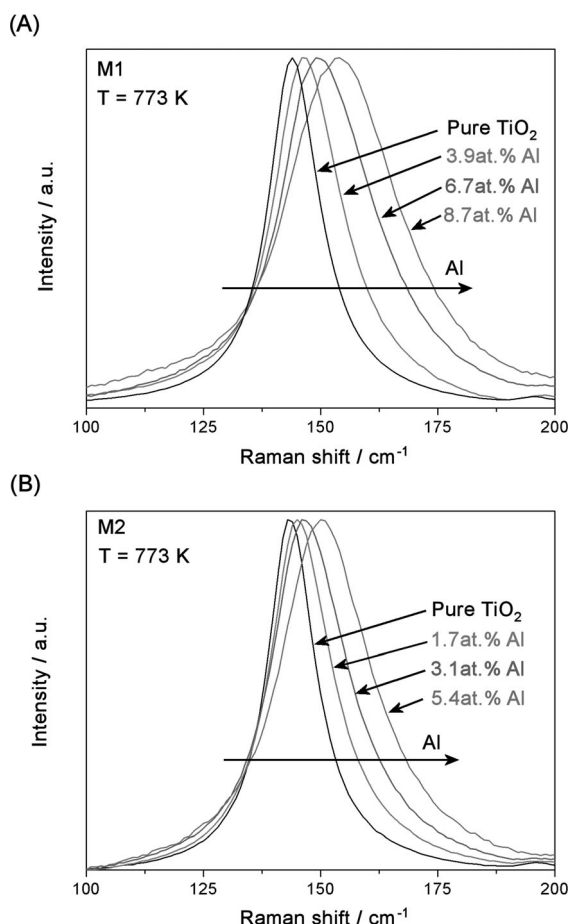| T_a [K]	Al/(Al+Ti) [at%]					
	0.0	1.7	3.1	5.4	9.1	14.3	15.4
773	anatase	anatase	anatase	anatase	low crystallinity	low crystallinity	low crystallinity
973	rutile	anatase	anatase	anatase	anatase	anatase	anatase
1173	rutile	rutile	rutile	anatase/rutile (40% < f_A < 60%)	anatase/rutile (40% < f_A < 60%)	anatase/rutile (40% < f_A < 60%)	anatase/rutile (40% < fA < 60%)

Figure 3. Shift in the $E_g(1)$ band in the Raman spectra for samples synthesized by a) method M1 and b) method M2.

Figure 4. Redshift in the diffuse reflectance UV/Vis spectra as a function of the annealing temperature for samples synthesized by both methods

Figure 3 shows a blueshift in the band of the $E_g(1)$ vibrational mode of the anatase phase in the Al-doped TiO_2 samples. This effect was observed for both methods of synthesis. The substitution of the Ti^{4+} ions by Al^{3+} generates distortions in the anatase structure. Given that the radius of Al^{3+} (0.51 Å) is smaller than that of Ti^{4+} (0.68 Å), the substitution of Ti^{4+} by Al^{3+} occurs, but this produces tensions and distortions in the crystalline lattice due to the difference in the electronegativities, ionic radii, and the oxidation states.[78] This produces oxygen vacancies to maintain the local charge neutrality.[38] These distortions cause the shift in the Raman bands, as reported previously.[37,38]

2.5 UV/Vis Spectroscopy

The UV/Vis spectra, in the diffuse reflectance mode, were recorded to characterize the light absorption properties of the synthesized samples. The annealing temperature is known to affect light absorption.[12,79] Figure 4 shows portions of the reflectance spectra for some synthesized samples considered as representatives, for which we can observe the influence of the annealing temperature. A redshift in the spectra is observed as the annealing temperature increases, which indicates a decrease in the band-gap energy.
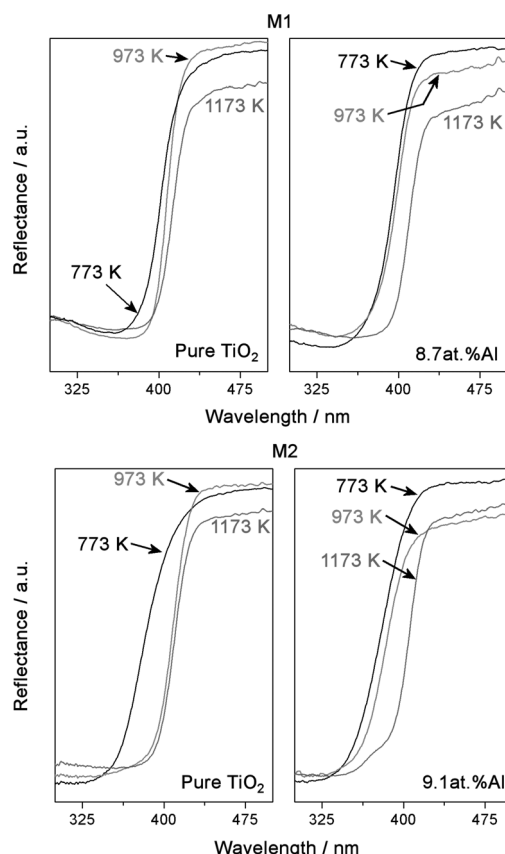
The band-gap energy was calculated by using the Kubelka–Munk function and a Tauc plot. For diffuse reflectance spectra, the Kubelka–Munk function is [Eq. (7)]:

$$f(R) = \frac{(1-R)^2}{2R} \qquad (7)$$

in which R is the reflectance. The plot for a semiconductor of $[f(R)h\nu]^n$ versus $h\nu$ shows a linear region for $n = 2$ and for $n = \frac{1}{2}$ if the band gap is determined by indirect or direct transition, respectively.[80,81] So, as reported in the literature, the plot of $[f(R)h\nu]^{1/2}$ versus $h\nu$ for TiO_2 shows a linear region that satisfies Equation (8):

$$[f(R)h\nu]^{1/2} = K(h\nu - E_g) \qquad (8)$$

in which E_g is the band-gap energy, K is a specific constant for each semiconductor, and $h\nu$ is the photon energy. Table S1 shows the band-gap values obtained. In general, the values obtained were between 2.91 and 3.23 eV, so the changes in the band-gap energy for the Al-doped TiO_2 samples synthesized by both methods were slight. In turn, Figure 5 shows the evolution of the band-gap energy with respect to the annealing temperature (Figure 5a) and a comparison for both methods (Figure 5b). In both methods of synthesis, the band-gap energy decreased as the annealing temperature was increased
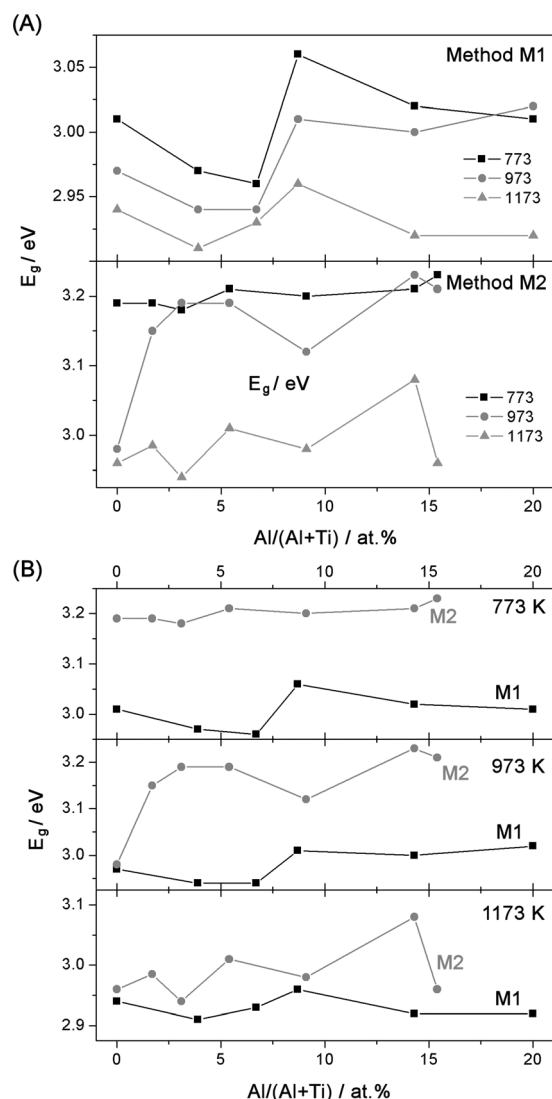
Figure 5. Evolution of the band-gap energy as a function of a) the atomic percentage of Al and b) the annealing temperature for samples synthesized by both methods.
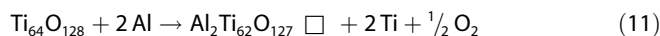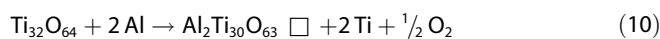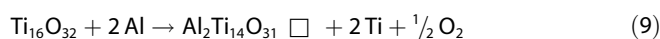
for each level of doping. This might be because as the temperature rises, the crystallite size increases (see Table 2), and this greater size implies a decrease in the band gap.[12] Furthermore, the temperature increase leads to an increased proportion of the rutile phase, especially at 1173 K, and the rutile phase is known to have a smaller band gap than the anatase phase.[82] The rutile phase also generates bigger crystallites, which decreases the band gap. These small modifications in the band-gap values are due to changes in the properties of the crystalline materials generated by doping and are not due to the introduction of the dopant into the structure, which does not generate changes in the semiconductor band structure. This idea is corroborated by the XPS results, which did not show any modification of the valence band maximum, and is also validated by the theoretical calculations shown below. Finally, it is possible to see that the band-gap values obtained for the samples synthesized with method M2 are higher than those for the samples synthesized with method M1. This may

be due to the lower crystallinity of the samples synthesized with method M2, as discussed above.

2.6 Energetics Considerations from a Theoretical Viewpoint

On the basis of the results of the experimental characterization, we performed theoretical calculations to gain a deeper understanding of the effect of Al doping on the structural and electronic properties of anatase TiO_2. The anatase phase was chosen because it is the predominant phase in the samples, as described above. The XPS results indicated the existence of Ti^{4+} and Al^{3+} and the negligible appearance of Ti^{3+} species. Thus, in our calculations, two Al^{3+} atoms substituted two Ti^{4+} atoms in anatase taking into account the equivalent sites. It is important to reiterate that the substitution of Al^{3+} implies the generation of oxygen vacancies to conserve local charge neutrality. Thus, we optimized the structures of $Al_2Ti_{62}O_{127}$, $Al_2Ti_{30}O_{63}$, and $Al_2Ti_{14}O_{31}$ and studied the formation and relative positions of the oxygen vacancies.

To gain insight into the energetics involved in the formation of the vacancies, we calculated the energy of the formal reactions [Eqs. (9)–(11)]:

$$Ti_{16}O_{32} + 2\,Al \rightarrow Al_2Ti_{14}O_{31}\,\square\, + 2\,Ti + {}^1\!/_2\,O_2 \qquad (9)$$

$$Ti_{32}O_{64} + 2\,Al \rightarrow Al_2Ti_{30}O_{63}\,\square\, + 2\,Ti + {}^1\!/_2\,O_2 \qquad (10)$$

$$Ti_{64}O_{128} + 2\,Al \rightarrow Al_2Ti_{62}O_{127}\,\square\, + 2\,Ti + {}^1\!/_2\,O_2 \qquad (11)$$

in which $\square$ denotes an oxygen vacancy. To model the dopant–vacancy system, it is necessary to identify the optimal configuration for the dopant and vacancy within the supercell. We identified the first coordination shell around the dopant as the most stable site for the vacancy to occur.

The energy associated to those reactions (E_r) can be described as [Eq. (12)]:

$$E_r = E(\text{doped}) - E(\text{host}) + 2\mu_{Al} + \mu_O + 2\mu_{Ti} \qquad (12)$$

in which $E(\text{doped})$ is the total energy of the system containing the Al atoms, $E(\text{host})$ is the total energy of the host cell, and μ_{Al}, μ_{Ti}, and μ_O are the chemical potentials of Al, Ti, and O respectively.[83,84] The value of μ_{Al} is calculated from the energy of an atom in bulk metal aluminum as in previous work for W.[83] The values of μ_{Ti} and μ_O are determined from Equations (13)–(15):[85–87]

$$\mu_{Ti} + 2\mu_O = \mu_{TiO_2} \qquad (13)$$

$$\mu_O = \frac{1}{2}E(O_2) + \mu'_O \qquad (14)$$

$$\mu'_O = \frac{1}{2}k_B T \ln\left(\frac{p}{p_0}\right) \qquad (15)$$

in which $E(O_2)$ is the total energy of an isolated oxygen molecule in a triplet state, k_B is the Boltzmann constant, and p is the pressure.
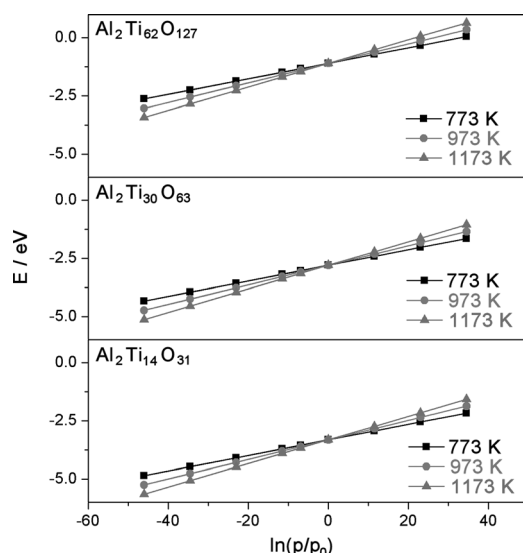
Figure 6. Dependence of the formation energy versus oxygen pressure as ln (p/p_0) at 773, 973, and 1173 K.

Figure 6 illustrates the dependence of the formation energy versus oxygen pressure as ln (p/p_0) at the experimental temperatures of 773, 973, and 1173 K. The reaction energies under the particular case of oxygen-rich conditions, that is, (p/p_0) = 1, for the most stable configuration of $Al_2Ti_{62}O_{127}$, $Al_2Ti_{30}O_{63}$, and $Al_2Ti_{14}O_{31}$ are −1.1, −2.8, and −3.3 eV, respectively. Figure 6 and the data above suggest that the generation of oxygen vacancies is favored under the experimental conditions.

2.7 Structure and Local Geometry Analysis

The local geometry for the most stable configuration of the optimized $Al_2Ti_{62}O_{127}$, $Al_2Ti_{30}O_{63}$, and $Al_2Ti_{14}O_{31}$ structures is shown in Figure 7 and Figure S5. As Figure 7 shows, the generation of an oxygen vacancy causes a distortion in the structure, as observed experimentally from the XRD and Raman spectroscopy results for the doped TiO_2 samples. The Al–□–Al distance (d_1 in Figure 7) increased from 9 to 11% relative to the

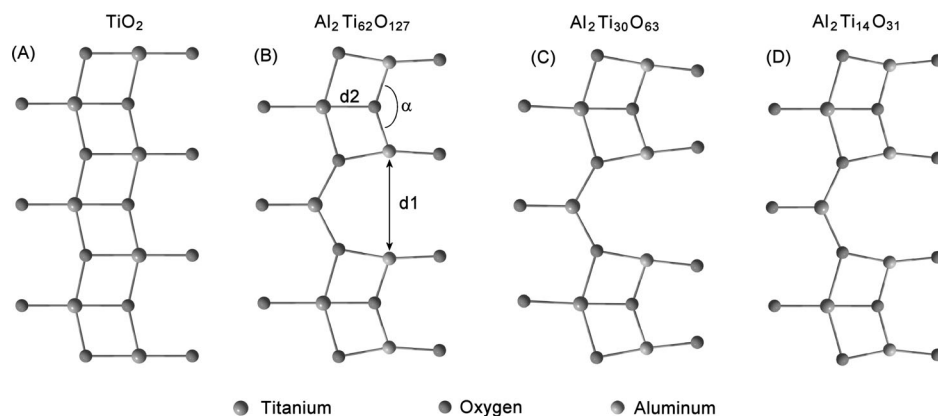same distance in bulk TiO_2 as the proportion of Al in the samples increased. Likewise, the Al–O–Al angle (α in Figure 7) decreased in the order 4.9, 5.5, and 6.6° with regard to the pure TiO_2.

Furthermore, in general, there was a reduction of 1.5% in the Ti–O distances around the vacancy (d_2 in Figure 7).

2.8 Charge Density and Electron Localization Function Study

The analysis of the charge density and the electron localization function (ELF) provides a reasonable explanation for the results. Figure 8 shows a 2D map of the charge densities and ELF of the anatase and doped structures for which the changes observed around the vacancy will be discussed. As a representative structure to discuss the changes, we chose the theoretical structure with the highest percentage of doping (12.5 at%), which was $Al_2Ti_{14}O_{31}$ (Figure 7 d). The 2D maps corresponding with the structures $Al_2Ti_{62}O_{127}$ and $Al_2Ti_{30}O_{63}$ are given in Figure S6.

As Figure 8 shows doping generated changes in the charge density. The most significant changes around the vacancy for $Al_2Ti_{14}O_{31}$ are highlighted in Figure 8 c as dotted squares. Comparing the charge density corresponding with the Ti–O bonds within the squares (Figure 8 c) with its anatase counterpart (Figure 8 a), a stronger Ti–O bond is observed for the $Al_2Ti_{14}O_{31}$ structure than for the TiO_2 one.

On the one hand, the Bader charges for Ti corroborate the existence of Ti^{4+} in TiO_2 and $Al_2Ti_{14}O_{31}$. The Bader charge value obtained was roughly 2.3–2.4 a.u., and this is a good fit with that reported in the literature for this species.[88] Furthermore, a considerable increase in the negative charge of the oxygen atoms was observed around the vacancy with a value of about −1.2 a.u. for TiO_2 to a value of around −1.4 a.u. for $Al_2Ti_{14}O_{31}$. This slight increase in the negative charge was also observed in the oxygen included in the smallest square in Figure 8 c. However, although its negative charge is slightly lower to balance the overall charge, for the rest of the oxygen atoms in the $Al_2Ti_{14}O_{31}$ structure the Bader charge was around −1.2 a.u., which is similar to that obtained for the oxygen atoms in TiO_2.

This indicates that upon generation of the vacancy, the negative charge is distributed around it to compensate the charge, which strengthens the Ti–O bond, and this explains why the distance decreases (d_2 in Figure 7). The increased strength of the Ti–O bond leads to a reduction in the Al–O–Al angle (α in Figure 7), which thus increases the Al–□–Al distance (d_1 in la Figure 7). The ELF for $Al_2Ti_{14}O_{31}$ (Figure 8 d) shows a value of 0 in the vacancy site, which implies that electrons are fully delocalized or that there are no electrons in that
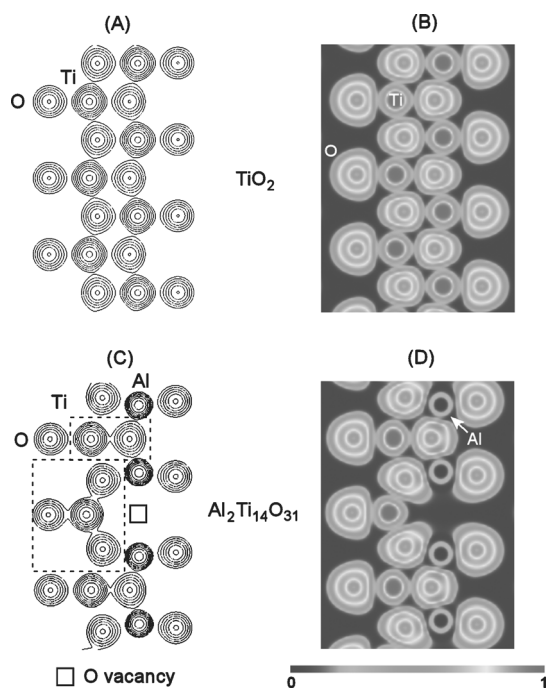

Figure 7. The local geometry for the most stable configuration of a) bulk anatase, b) $Al_2Ti_{62}O_{127}$, c) $Al_2Ti_{30}O_{63}$, and d) $Al_2Ti_{14}O_{31}$.

Figure 8. Charge density and ELF contour plots of a b) pure and c,d) Al-doped anatase ($Al_2Ti_{14}O_{31}$).

place. Thus, the ELF corroborates that the negative charge is distributed and divided by O^{2-} around the vacancy for $Al_2Ti_{14}O_{31}$ (Figure 8d), in contrast to TiO_2 (Figure 8b). Finally, the aluminum had a Bader charge of around 2.4 a.u., which is similar to the values reported for Al^{3+} in $MgAl_2O_4$.[89]

In our study, although experimentally there was no evidence for the appearance of Ti^{3+} species,[65] for comparison purposes the charge density map and ELF corresponding to the $AlTi_7O_{15}$ structure are included (Figure 9). For this structure, the Ti^{3+} species appears as a consequence of the charge compensation. The electronic situation for the $AlTi_7O_{15}$ structure differs greatly from that of the $Al_2Ti_{14}O_{31}$ structure. Thus, its density map (Figure 9a) is different to that of TiO_2 and $Al_2Ti_{14}O_{31}$ (Figure 8). For $AlTi_7O_{15}$, the Bader charge value obtained for Ti was about 2.1 a.u., which indicates the appearance of the Ti^{3+} species, and this is in line with previous values obtained for
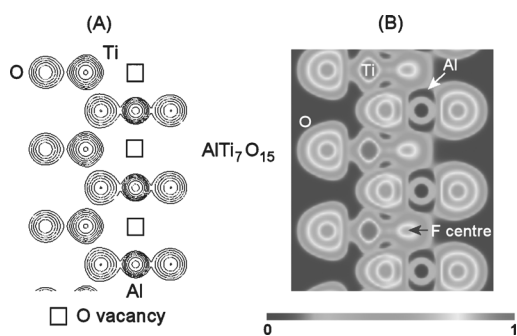

Figure 9. Charge density and ELF contour plots of Al-doped anatase ($AlTi_7O_{15}$).

this species.[88] The Bader charge for Al was approximately 2.3 a.u. and those for the oxygen atoms around the vacancy on the left and right were about -1.5 and -1.3 a.u., that is, the negative charge was localized in the zone to the left of the vacancy (Figure 9a), which compensates the charge deficiency. This effect can be seen more clearly in the ELF for $AlTi_7O_{15}$ (Figure 9b). The topological features of the ELF for the Al-doped structure with Ti^{3+} (Figure 9b) are different than those obtained for the Ti^{4+} structures (Figure 8b,d). The ELF is high in the region of the oxygen vacancy. Thus, upon vacancy creation, the electrons prefer to remain localized at the vacancy site to form an F center. It is important to remember that these changes in the electronic density can be detected by using experimental techniques such as XPS. As discussed above, the Ti^{3+} species was not detected experimentally, so the $AlTi_7O_{15}$ structure was not obtained experimentally and was included in this study for comparative purposes to confirm the conclusions reached experimentally.

2.9 Density of States and Projected Density of States Analysis

Finally, the study of the band gap corroborates that the structures optimized with Ti^{4+} and the presence of oxygen vacancies give a good qualitative description of the system used in the study. Our experimental results show that the band gap of the Al-doped samples remains largely unchanged relative to that of TiO_2 and that the small modifications were caused by changes in the crystalline properties of the nanoparticles (size, relative fraction of each phase present) and not by modification of the band levels due to the introduction of Al into the structure. From a theoretical viewpoint, the results obtained are consistent. We will discuss the electronic structure in terms of the density of states (DOS) and the projected density of states (PDOS). Figure 10a compares the DOS of TiO_2 with the Al-doped TiO_2 structures. Figure 10a shows that higher concentrations of Al do not lead to a variation in the DOS compared with TiO_2, which indicates that the band gap remains practically constant, as is the case experimentally. Figure 10b shows the PDOS analysis of Ti, Al, and O for the $Al_2Ti_{14}O_{31}$ structure. It indicates that the valence band of $Al_2Ti_{14}O_{31}$ is mostly composed of O 2p states and the conduction band is dominated by Ti 3d states. This result was also observed for pure TiO_2 (Figure S7). There was a residual contribution of the Al states to both the conduction band and the valence band, which is consistent with the results obtained by XPS. These results were also observed in the PDOS of the $Al_2Ti_{62}O_{127}$ and $Al_2Ti_{30}O_{63}$ structures (Figure S7).

In this analysis, it was also possible to compare our structures with those in which Ti^{3+} species might be present. In this case, its presence should be reflected in the band-gap value, as shown by the theoretical results in Figure 11, which compares the DOS of TiO_2 and $Al_2Ti_{14}O_{31}$ with Ti^{4+} and that of $AlTi_7O_{15}$ with Ti^{3+}. The PDOS for $AlTi_7O_{15}$ is shown in Figure S8. As Figure 11 shows, the $AlTi_7O_{15}$ structure has a smaller band gap than TiO_2 and $Al_2Ti_{14}O_{31}$. Bearing in mind that the synthesized Al-doped samples did not have a smaller band gap than

(A)

(B)

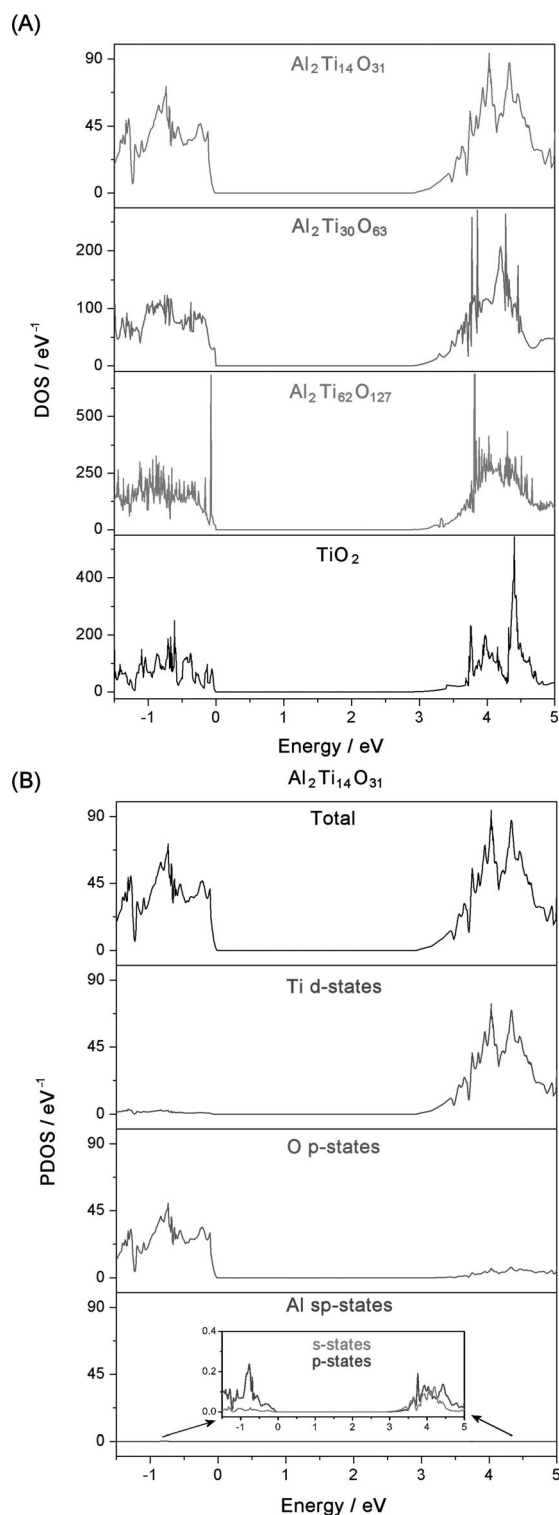**Figure 10.** a) DOS for pure anatase TiO_2, $Al_2Ti_{62}O_{127}$, $Al_2Ti_{30}O_{63}$, and $Al_2Ti_{14}O_{31}$. b) PDOS for $Al_2Ti_{14}O_{31}$. The top panel corresponds to the total DOS, and the middle and bottom panels correspond to the Ti, O, and Al projected d, p, and sp states, respectively.

the pure TiO_2 samples, it can be concluded that the presence of the Ti^{3+} species in the synthesized samples is negligible, as the experimental and theoretical results showed.
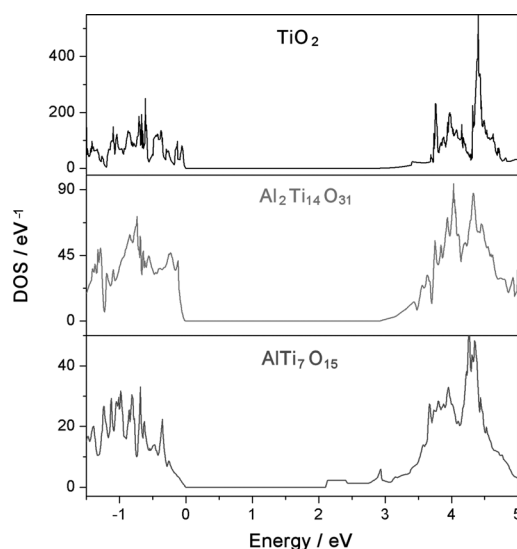

Figure 11. DOS for pure anatase TiO_2, $Al_2Ti_{14}O_{31}$, and $AlTi_7O_{15}$.

3. Conclusions

A study was performed of Al-doped TiO_2 nanoparticles. These were synthesized by using two different methods and were extensively characterized with several technical instruments. High internal doping of the TiO_2 structure was obtained upon substituting the Ti^{4+} ions with Al^{3+} ions. Furthermore, several of the properties of the nanoparticles depended on the method of synthesis used. The levels of doping and the crystallinity of the nanoparticles were affected by the method of synthesis, and differences were observed between the methods. However, the nanoparticles had some properties in common. As stated above, internal doping was achieved in both cases, and XPS showed that the predominant Ti species was Ti^{IV}, so the introduction of Al^{III} generated oxygen vacancies in the structure of TiO_2. In turn, these vacancies depended on the level of doping, a characteristic that makes these synthesized nanomaterials of interest for use in photocatalytic applications. Also, UV/Vis spectroscopy indicated that the band-gap energy of Al-doped TiO_2 was similar to that of TiO_2. This result was supported by XPS, which showed that the valence band did not contribute significantly to the Al orbitals. From a theoretical viewpoint, the band gap of the optimized Al-doped TiO_2 structures corresponded to that of the experimental structures and was similar to that of TiO_2. This is because the valence band was mostly composed of O 2p states and the conduction band was dominated by Ti 3d states, the same as TiO_2. Furthermore, the contribution of the states of Al to the valence band and conduction was insignificant. The theoretical results were consistent with the experimental XPS data and confirmed the presence of Ti^{4+} and Al^{3+} species. Charge density and ELF studies indicated that the generation of oxygen vacancies in the structures of Al-doped TiO_2 caused the negative charge to be distributed among the oxygen atoms around the vacancies. This implied a strengthening of the Ti–O bonds around the vacancy relative to the same bond in pure TiO_2.

Experimental and Computational Section

Synthesis

Two methods were used for the synthesis of the Al-doped TiO_2 nanoparticles. The nanoparticles synthesized were broadly characterized, and the results obtained by both methods of synthesis were compared. The methods and the characterization techniques used are described below.

Method M1: This method was based on a low-temperature hydrolysis reaction by using titanium butoxide as a precursor. This method was previously described in the literature,[25] and it can be summarized as follows: Deionized water (100 mL) was cooled at 277 K. During the cooling time, a stoichiometric amount of aluminum isopropylate (purity 98%, Panreac) was added to obtain a theoretical Al/TiO_2 weight doping of 1, 2, 2.5, 5.0, and 7.5 wt%. Titanium butoxide (10 mL, purity 97%, Sigma–Aldrich) was added dropwise under magnetic stirring. Then, the solution was homogenized for 30 min and HNO_3 (4 mL, purity 65%, Merck Suprapur) was added. The solution was stirred for 2 h, and then the excess amount of solvent was evaporated under vacuum at 333 K by using a rotavapor and after at 373 K on a hotplate until its total removal. Finally, the pure and Al-doped TiO_2 samples were annealed at 773, 973, and 1173 K in air for 1 h.

Method M2: This method was based on a water-controlled hydrolysis reaction by using titanium isopropoxide as a precursor of TiO_2. The procedure can be described as follows: A stoichiometric amount of $Al_2(SO_4)_4 \cdot 18 H_2O$ (purity 99%, Merck) was dissolved in water (7 mL) to obtain a theoretical Al/TiO_2 weight doping of 1, 2, 2.5, 5.0, 7.5, and 10 wt%. The solution was added dropwise under sonication (130 W, 20 Hz) to titanium isopropoxide (10 mL, purity 98%, Acros Organics) over 5 min; the temperature of the reaction system was 323 K and the acidity was pH 4. Finally, the pure and Al-doped TiO_2 samples were annealed at 773, 973, and 1173 K in air for 2 h, and the solvent removal was performed by means of a progressive increase in the oven temperature until the annealing temperature.

Characterization

Several instrumental techniques were used to characterize the different properties of the nanoparticles synthesized, such as their composition, structure, crystalline phases, and electronic properties. Pure TiO_2 samples synthesized by using both methods were characterized to determine the effect of doping on the structure and properties of TiO_2. So, inductively coupled plasma atomic emission spectroscopy (ICP-AES) was used to determine the amount of Al in the doped TiO_2. This was performed by using an Iris Intrepid spectrometer, supplied by Thermo Elemental. Moreover, the structural analysis was performed by using several techniques. X-ray diffraction (XRD) was used to determine the main crystalline phase of the samples. Some properties such as the average crystallite size, the specific surface area, the volume of the unit cell, and the lattice parameters were determined semiquantitatively from the XRD patterns obtained. The patterns were registered by using a diffractometer supplied by Bruker, model D8 Advanced, with CuKα radiation. The scan conditions were from 20 to 70° in 2θ with a resolution of 0.05°, 4 kV, and 40 mA. The structural study was completed by using Raman spectroscopy. The Raman spectra were collected in a backscattering geometry by using a Jobin Yvon U1000 double monochromator equipped with a Hamamatsu R-943 photomultiplier and a DPSS 473 nm laser supplied by Cobolt. Moreover, X-ray photoelectron spectroscopy (XPS) was used to

study the chemical bonding states and the chemical compositions of the samples. The spectra were obtained by using a Kratos Axis UltraDLD spectrometer, with monochromated AlKα radiation (1486.6 eV) and a 20 eV pass energy. The binding energy scale was referenced to the C 1s signal at 284.8 eV and is given with an accuracy of 0.01 eV. Finally, UV/Vis spectroscopy in the reflectance diffuse mode was performed to study the optical properties. In addition, the band-gap energy was determined. The spectra were collected by using a system assembled in our laboratory composed of an integrating sphere supplied by Spectra Tech, a USB2000+ spectrometer from Ocean Optics, and a Xe lamp, model ASB-XE-175, supplied by Spectral Products.

Computational Framework

DFT-periodic calculations were performed by using the Vienna Ab Initio Simulation Package (VASP)[42–45] with the projector-augmented wave (PAW) method.[46,47]

The number of plane waves in VASP was controlled by a cut-off energy, which in our calculations was set to $E_{cut} = 500$ eV to satisfactorily describe the system.[86] The electron exchange and correlation were treated within the local density approximation (LDA).[90] Both the cell shape and atomic positions were optimized by using a conjugate-gradient algorithm, for which the iterative relaxation of the atomic positions was stopped if the forces on the atoms were less than 0.01 eV Å^{-1}. Also, a Gaussian smearing with $k_B T = 0.1365$ eV was applied.

The anatase structure was characterized by the tetragonal I4/amd space group.[91] A Monkhorst–Pack grid[92] of $4 \times 4 \times 2$ k-points mesh for sampling the Brillouin zone for anatase bulk (12 atoms) was enough to reach negligible changes in the optimized cell parameters and energy. The resulting cell parameters were $a = 3.749$ Å, $c = 9.502$ Å for LDA, in agreement with the experimental values ($a = 3.782$ Å, $c = 9.502$ Å).[91]

The $Ti_{64}O_{128}$ (192 atoms), $Ti_{32}O_{64}$ (96 atoms), and $Ti_{16}O_{32}$ (48 atoms) cells were optimized as anatase models for doping. The implantation of Al into the structure was performed on substitutional positions. The Al atom substituted the Ti atom in TiO_2 taking into account the equivalent sites. Close attention was paid to oxygen vacancies and reporting the most stable configuration for each composition. Thus, the $Al_2Ti_{62}O_{127}$ (191 atoms), $Al_2Ti_{30}O_{63}$ (94 atoms), and $Al_2Ti_{14}O_{31}$ (47 atoms) structures were optimized to simulate the experimental stoichiometries within the most interesting range of doping. The selected structures were suitable to qualitatively represent the wide range of experimental concentrations within DFT with a periodic boundary condition framework. The density of states (DOS) and projected density of states (PDOS) for the relaxed structures were obtained by using the tetrahedron method with Blöchl corrections[93] and a mesh of $8 \times 8 \times 8$ k-points. For all the systems, DFT$+U$[94] calculations were performed to take into account the on-site Coulomb interaction by applying a U value of 5 eV.[95–97]

Bader charge analysis was performed by using the Bader program[48–50] from the Henkelman Group at the University of Texas. Two-dimensional charge densities were plotted by using the VESTA software.[98] Electron localization function (ELF)[51–55] images and structure images were obtained by using the vaspview software and ChemCraft 1.6.[99,100]

To calculate reaction energies, the energy of the O_2 molecule and Al metal were obtained with VASP by using the same PAW poten-

tials, cut-off energy, and other precision parameters as those in the other calculations.

[1] A. C. Lee, R. H. Lin, C. Y. Yang, M. H. Lin, W. Y. Wang, *Mater. Chem. Phys.* **2008**, *109*, 275–280.
[2] Z. Y. Weng, H. Guo, X. M. Liu, S. L. Wu, K. W. K. Yeung, P. K. Chu, *RSC Adv.* **2013**, *3*, 24758–24775.
[3] A. Fujishima, K. Honda, *Nature* **1972**, *238*, 37.
[4] M. Ni, M. K. H. Leung, D. Y. C. Leung, K. Sumathy, *Renewable Sustainable Energy Rev.* **2007**, *11*, 401–425.
[5] T. Inoue, A. Fujishima, S. Konishi, K. Honda, *Nature* **1979**, *277*, 637–638.
[6] T. Yui, A. Kan, C. Saitoh, K. Koike, T. Ibusuki, O. Ishitani, *ACS Appl. Mater. Interfaces* **2011**, *3*, 2594–2600.
[7] Z. H. Zhao, J. M. Fan, M. M. Xie, Z. Z. Wang, *J. Cleaner Prod.* **2009**, *17*, 1025–1029.
[8] X. H. Xia, Z. H. Jia, Y. Yu, Y. Liang, Z. Wang, L. L. Ma, *Carbon* **2007**, *45*, 717–721.
[9] Y. Kohno, T. Yamamoto, T. Tanaka, T. Funabiki, *J. Mol. Catal. A* **2001**, *175*, 173–178.
[10] C. C. Lo, C. H. Hung, C. S. Yuan, J. F. Wu, *Solar Energy Materials and Solar Cells.* **2007**, *91*, 1765–1774.
[11] S. Y. Liu, G. C. Liu, Q. G. Feng, *J. Porous Mater.* **2010**, *17*, 197–206.
[12] G. H. Wang, L. Xu, J. Zhang, T. T. Yin, D. Y. Han, *Int. J. Photoenergy* **2012**, 265760.
[13] B. O'Regan, M. Grätzel, *Nature* **1991**, *353*, 737–740.
[14] D. H. Kim, W. M. Seong, I. J. Park, E. S. Yoo, S. S. Shin, J. S. Kim, H. S. Jung, S. Lee, K. S. Hong, *Nanoscale* **2013**, *5*, 11725–11732.
[15] M. Toivola, J. Halme, K. Miettunen, K. Aitola, P. D. Lund, *Int. J. Energy Res.* **2009**, *33*, 1145–1160.
[16] O. Kuzmych, K. Nonomura, E. M. J. Johansson, T. Nyberg, A. Hagfeldt, M. Skompska, *Thin Solid Films* **2012**, *522*, 71–78.
[17] J. Durantini, P. P. Boix, M. Gervaldo, G. M. Morales, L. Otero, J. Bisquert, E. M. Barea, *J. Electroanal. Chem.* **2012**, *683*, 43–46.
[18] R. Dholam, N. Patel, M. Adami, A. Miotello, *Int. J. Hydrogen Energy* **2009**, *34*, 5337–5346.
[19] M. A. Khan, S. I. Woo, O. B. Yang, *Int. J. Hydrogen Energy* **2008**, *33*, 5345–5351.
[20] J. H. Park, S. Kim, A. J. Bard, *Nano Lett.* **2006**, *6*, 24–28.
[21] B. Zhou, M. Schulz, H. Y. Lin, S. I. Shah, J. H. Qu, C. P. Huang, *Appl. Catal., B* **2009**, *92*, 41–49.
[22] Y. Q. Wu, G. X. Lu, S. B. Li, *J. Phys. Chem. C* **2009**, *113*, 9950–9955.
[23] M. F. L. Hou, F. B. Li, R. F. Wan, H. F. Zhou, G. Y. Xie, *J. Chinese Rare Earth Soc.* **2004**, *22*, 75–80.
[24] Y. Izumi, T. Itoi, S. Peng, K. Oka, Y. Shibata, *J. Phys. Chem. C* **2009**, *113*, 6706–6718.
[25] T. Aguilar, J. Navas, R. Alcántara, C. Fernández-Lorenzo, J. J. Gallardo, G. Blanco, J. Martín-Calleja, *Chem. Phys. Lett.* **2013**, *571*, 49–53.
[26] S. M. Yang, S. P. Guo, D. L. Xu, H. B. Xue, H. Z. Kou, J. C. Wang, G. H. Zhu, *J. Fluorine Chem.* **2013**, *150*, 78–84.
[27] J. W. Li, X. Chen, N. Ai, J. M. Hao, Q. Chen, S. Strauf, Y. Shi, *Chem. Phys. Lett.* **2011**, *514*, 141–145.
[28] Y. D. Duan, N. Q. Fu, Q. Zhang, Y. Y. Fang, X. W. Zhou, Y. Lin, *Electrochim. Acta* **2013**, *107*, 473–480.
[29] K. H. Ko, Y. C. Lee, Y. J. Jung, *J. Colloid Interface Sci.* **2005**, *283*, 482–487.
[30] H. J. Tian, L. H. Hu, C. N. Zhang, W. Q. Liu, Y. Huang, L. Mo, L. Guo, J. Sheng, S. Y. Dai, *J. Phys. Chem. C* **2010**, *114*, 1627–1632.
[31] X. J. Lu, X. L. Mou, J. J. Wu, D. W. Zhang, L. L. Zhang, F. Q. Huang, F. F. Xu, S. M. Huang, *Adv. Funct. Mater.* **2010**, *20*, 509–515.
[32] W. W. Wu, S. Y. Dai, L. H. Hu, L. Y. Liang, K. J. Wang, *Chin. Phys. Lett.* **2006**, *23*, 2288–2291.
[33] J. Navas, C. Fernandez-Lorenzo, T. Aguilar, R. Alcantara, J. Martin-Calleja, *Phys. Status Solidi A* **2012**, *209*, 378–385.
[34] Q. Zhao, P. Wu, B. L. Li, E. Y. Jiang, *Physica B + C* **2012**, *407*, 171–174.
[35] S. S. Lin, D. K. Wu, *Ceram. Int.* **2010**, *36*, 87–91.
[36] A. K. P. D. Savio, J. Fletcher, F. C. R. Hernandez, *Ceram. Int.* **2013**, *39*, 2753–2765.
[37] M. S. Kang, *Mater. Lett.* **2005**, *59*, 3122–3127.
[38] M. I. Zaki, A. Katrib, A. I. Muftah, T. C. Jagadale, M. Ikram, S. B. Ogale, *Appl. Catal., A* **2013**, *452*, 214–221.
[39] A. Iwaszuk, M. Nolan, *J. Phys. Condens. Matter* **2011**, *23*, 334207.
[40] R. Shirley, M. Kraft, O. R. Inderwildi, *Phys. Rev. B* **2010**, *81*, 075111.
[41] F. Gracia, J. P. Holgado, A. Caballero, A. R. Gonzalez-Elipe, *J. Phys. Chem. B* **2004**, *108*, 17466–17476.
[42] G. Kresse, J. Hafner, *Phys. Rev. B* **1993**, *47*, 558–561.
[43] G. Kresse, J. Hafner, *Phys. Rev. B* **1994**, *49*, 14251–14269.
[44] G. Kresse, J. Furthmüller, *Comput. Mater. Sci.* **1996**, *6*, 15–50.
[45] G. Kresse, J. Furthmüller, *Phys. Rev. B* **1996**, *54*, 11169–11186.
[46] P. E. Blochl, *Phys. Rev. B* **1994**, *50*, 17953–17979.
[47] G. Kresse, D. Joubert, *Phys. Rev. B* **1999**, *59*, 1758–1775.
[48] W. Tang, E. Sanville, G. Henkelman, *J. Phys. Condens. Matter* **2009**, *21*, 084204.
[49] E. Sanville, S. D. Kenny, R. Smith, G. Henkelman, *J. Comput. Chem.* **2007**, *28*, 899–908.
[50] G. Henkelman, A. Arnaldsson, H. Jonsson, *Comput. Mater. Sci.* **2006**, *36*, 354–360.
[51] A. D. Becke, K. E. Edgecombe, *J. Chem. Phys.* **1990**, *92*, 5397–5403.
[52] B. Silvi, A. Savin, *Nature* **1994**, *371*, 683–686.
[53] B. Silvi, C. Gatti, *J. Phys. Chem. A* **2000**, *104*, 947–953.
[54] A. Savin, O. Jepsen, J. Flad, O. K. Andersen, H. Preuss, H. G. Vonschnering, *Angew. Chem. Int. Ed. Engl.* **1992**, *31*, 187–188; *Angew. Chem.* **1992**, *104*, 186–188.
[55] A. Savin, A. D. Becke, J. Flad, R. Nesper, H. Preuss, H. G. Vonschnering, *Angew. Chem. Int. Ed. Engl.* **1991**, *30*, 409–412; *Angew. Chem.* **1991**, *103*, 421–424.
[56] K. Chiang, R. Amal, T. Tran, *Adv. Environ. Res.* **2002**, *6*, 471–485.
[57] C. Y. Tsai, T. H. Kuo, H. C. Hsi, *Int. J. Photoenergy* **2012**, 874509.
[58] B. E. Warren, *X-ray Diffraction*, Dover Publications, Inc., New York, **1990**.
[59] L. Xu, M. P. Garrett, B. Hu, *J. Phys. Chem. C* **2012**, *116*, 13020–13025.
[60] M. A. Shui, Y. Song, Q. C. Wang, Y. L. Ren, *Curr. Appl. Phys.* **2010**, *10*, 1360–1365.
[61] A. Maurya, P. Chauhan, S. K. Mishra, R. K. Srivastava, *J. Alloys Compd.* **2011**, *509*, 8433–8440.
[62] M. C. Biesinger, L. W. M. Lau, A. R. Gerson, R. S. C. Smart, *Appl. Surf. Sci.* **2010**, *257*, 887–898.
[63] A. K.-V. A. V. Naumkin, S. W. Gaarenstroom, C. J. Powell, in *NIST Standard Reference Database 20*, Version 4.1, Gaithersburg, **2012**.
[64] W. M. R. C. D. Wagner, L. E. Davis, J. F. Moulder, *Handbook of XPS*, PerkinElmer Corp., Minnesota, **1979**.
[65] F. Zuo, L. Wang, T. Wu, Z. Y. Zhang, D. Borchardt, P. Y. Feng, *J Am Chem. Soc.* **2010**, *132*, 11856–11857.
[66] C. Z. Li, L. Y. Shi, D. M. Xie, H. L. Du, *J. Non-Cryst. Solids* **2006**, *352*, 4128–4135.
[67] N. Kruse, S. Chenakin, *Appl. Catal., A* **2011**, *391*, 367–376.
[68] S. W. Ryu, E. J. Kim, S. K. Ko, S. H. Hahn, *Mater. Lett.* **2004**, *58*, 582–587.
[69] B. Schumacher, V. Plzak, J. Cai, R. J. Behm, *Catal Lett.* **2005**, *101*, 215–224.
[70] H. M. Liu, W. S. Yang, Y. Ma, Y. Cao, J. N. Yao, J. Zhang, T. D. Hu, *Langmuir* **2003**, *19*, 3001–3005.
[71] Y. V. Zubavichus, Y. L. Slovokhotov, M. K. Nazeeruddin, S. M. Zakeeruddin, M. Grätzel, V. Shklover, *Chem. Mater.* **2002**, *14*, 3556–3563.
[72] S. K. Joung, T. Amemiya, M. Murabayashi, K. Itoh, *J. Photochem. Photobiol. A* **2006**, *184*, 273–281.
[73] G. Colon, M. C. Hidalgo, G. Munuera, I. Ferino, M. G. Cutrufello, J. A. Navio, *Appl. Catal., B* **2006**, *63*, 45–59.

[74] J. G. Yu, G. H. Wang, B. Cheng, M. H. Zhou, *Appl. Catal., B* **2007**, *69*, 171–180.

[75] J. Wang, T. Ma, Z. H. Zhang, X. D. Zhang, Y. F. Jiang, W. Sun, R. H. Li, P. Zhang, *Ultrason. Sonochem.* **2007**, *14*, 575–582.

[76] S. K. S. Patel, N. S. Gajbhiye, S. K. Date, *J. Alloys Compd.* **2011**, *509*, S427–S430.

[77] N. R. Mathews, E. R. Morales, M. A. Cortes-Jacome, J. A. T. Antonio, *Sol Energy.* **2009**, *83*, 1499–1508.

[78] J. Emsley, *The Elements*, Clarendon Press, New York, **1998**.

[79] J. W. Shi, S. H. Chen, S. M. Wang, Z. L. Ye, P. Wu, B. Xu, *J. Mol. Catal. A: Chem.* **2010**, *330*, 41–48.

[80] L. Diamandescu, F. Vasiliu, D. Tarabasanu-Mihaila, M. Feder, A. M. Vlaicu, C. M. Teodorescu, D. Macovei, I. Enculescu, V. Parvulescu, E. Vasile, *Mater. Chem. Phys.* **2008**, *112*, 146–153.

[81] A. B. Murphy, *Sol. Energy Mater. Sol. Cells* **2007**, *91*, 1326–1337.

[82] A. K. Tripathi, M. K. Singh, M. C. Mathpal, S. K. Mishra, A. Agarwal, *J. Alloys Compd.* **2013**, *549*, 114–120.

[83] R. Long, N. J. English, *Appl. Phys. Lett.* **2009**, *94*, 132102–132104.

[84] R. Long, N. J. English, *Chem. Mater.* **2010**, *22*, 1616–1623.

[85] N. C. Wilson, I. E. Grey, S. P. Russo, *J. Phys. Chem. C* **2007**, *111*, 10915–10922.

[86] Y. Ortega, N. C. Hernandez, E. Menendez-Proupin, J. Graciani, J. F. Sanz, *Phys. Chem. Chem. Phys.* **2011**, *13*, 11340–11350.

[87] K. Reuter, M. Scheffler, *Phys. Rev. B* **2001**, *65*, 035406.

[88] H. R. Chauke, P. Murovhi, P. E. Ngoepe, N. H. de Leeuw, R. Grau-Crespo, *J. Phys. Chem. C* **2010**, *114*, 15403–15409.

[89] C. A. Gilbert, R. Smith, S. D. Kenny, S. T. Murphy, R. W. Grimes, J. A. Ball, *J. Phys. Condens. Matter* **2009**, *21*, 275406.

[90] J. P. Perdew, A. Zunger, *Phys. Rev. B* **1981**, *23*, 5048–5079.

[91] J. K. Burdett, T. Hughbanks, G. J. Miller, J. W. Richardson, J. V. Smith, *J. Am. Chem. Soc.* **1987**, *109*, 3639–3646.

[92] H. J. Monkhorst, J. D. Pack, *Phys. Rev. B* **1976**, *13*, 5188–5192.

[93] P. E. Blochl, O. Jepsen, O. K. Andersen, *Phys. Rev. B* **1994**, *49*, 16223–16233.

[94] S. L. Dudarev, G. A. Botton, S. Y. Savrasov, C. J. Humphreys, A. P. Sutton, *Phys. Rev. B* **1998**, *57*, 1505–1509.

[95] C. J. Calzado, N. C. Hernandez, J. F. Sanz, *Phys. Rev. B* **2008**, *77*, 045118.

[96] M. M. Branda, N. C. Hernandez, J. F. Sanz, F. Illas, *J. Phys. Chem. C* **2010**, *114*, 1934–1941.

[97] J. J. Plata, A. M. Marquez, J. F. Sanz, *J. Chem. Phys.* **2012**, *136*, 041101.

[98] K. Momma, F. Izumi, *J. Appl. Crystallogr.* **2011**, *44*, 1272–1276.

[99] T. B. Terriberry, D. F. Cox, D. A. Bowman, *Comput. Chem.* **2002**, *26*, 313–319.

[100] www.chemcraftprog.com.